Fano-type spectra and other interference effects in an all-dielectric nanoshell

2017 J. Opt. 19 075603

(http://iopscience.iop.org/2040-8986/19/7/075603)

IOP Publishing Journal of Optics
J. Opt. 19 (2017) 075603 (9pp) https://doi.org/10.1088/2040-8986/aa72ad

Fano-type spectra and other interference effects in an all-dielectric nanoshell

Srishti Garg and Murugesan Venkatapathi

Computational & Statistical Physics Laboratory, Department of Computational Sciences, Indian Institute of Science, Bangalore 560012, India

E-mail: murugesh@cds.iisc.ac.in

Received 30 December 2016, revised 2 May 2017
Accepted for publication 12 May 2017
Published 22 June 2017

Abstract

Large spectral variations in the extinction of nanostructures are important for many applications like optical antennas, cloaking materials, optical circuits and others. Such features in extinction spectra are typically attained using plasmonic particles and high-index or complex nanostructures. In this work, we show that large interference structures can manifest even in the extinction spectra of a single dielectric particle with a low relative refractive index (<2), and notably even as a spectral region of transparency and directional scattering of incident light. This is observed when the core and shell resonances of a layered spherical particle have overlaps with each other in the energy spectrum. Interference between the core and shell modes results in larger spectral features in magnitudes of the scattering constants a_n, b_n i.e. a strong enhancement of what is traditionally called the ripple structure in the extinction spectra of a dielectric particle. This effect is in addition to any possible overlap of electric resonances of two different mode numbers or the overlap of an electric and magnetic resonance, which have been shown to result in sharp asymmetric (Fano) resonances in the forward or backscattering spectra of a high-index or metallic particle.

Supplementary material for this article is available online

Keywords: Fano resonance, Mie theory, all-dielectric

(Some figures may appear in colour only in the online journal)

1. Introduction

Core–shell nanoparticles have been studied extensively in recent years for their high optical efficiencies, and due to the sensitivity of their optical properties to geometrical parameters [1, 2]. In plasmonic metal nanoparticles, the electromagnetic energy can be extremely localized with apparent near and far field optical properties. This property can be used in the modification of local emission properties, increasing the efficiency of absorption, and has many biological applications [3–5]. Nevertheless the large non-radiative losses in such metal particles discourage their use in bulk materials for many applications. Hence, discovering useful optical properties in non-plasmonic nanostructures is a significant direction of research in developing nanoscale materials [6]. One path towards realizing new useful optical properties is the excitation of higher-order modes of nanostructures like nanoshells [7–10].

Studies of layered nanospheres with an absorbing layer or core were motivated by meteorological applications many decades before the advent of plasmonics [11]. More recently, the tunable properties of plasmonic core–shell nanostructures have been studied for applications where low quality factors and dissipative losses are not an impediment. Non-intuitive properties of magnetic spheres like a negligible backscattering efficiency were predicted decades ago, [12] and recent experimental observations of certain cylindrical oligomers confirm such behavior [13–15]. But studies of dielectric particles have been mostly limited to large cylindrical and spherical microstructures for optical fiber communication and optical cavities that exploit whispering gallery modes, respectively [16–20]. Note that a weak interference structure in the extinction spectrum of homogeneous particles on the order of wavelength in size has been well known for some time [21]. This was understood as the spectral maxima and minima representing the

interference of the incident and forward-scattered light, and this effect has been used in microwave signal processing before [22]. Also, an asymmetric optical resonance for particles was predicted by van de Hulst earlier than its quantum-mechanical counterpart [23] and such a resonance was experimentally observed using nanospheres with a sharp absorption spectrum [24] before Fano resonances became well known in plasmonics. Plasmonic particles offer the possibility of sharp changes in the optical spectra when modes are strongly coupled by their dissipative currents. This is indicated by an overlap of resonance of two electric modes, e.g. a near overlap of peaks of the scattering constants [25].

However, we highlight that stronger interference structures can appear in spectra of some dielectric nanoshells with dimensions close to the wavelength of incident light, i.e $2\pi > kd > 1$, where k is the magnitude of the incident wavevector and d is the dimension of the layers. Spherical nanoshells in particular allow us to derive polarization-independent resonances. Transparencies where the optical efficiency of a large nanoparticle reduces to unity due to a minimal interaction with the incident field are equally significant spectral regions [26]. We show that such effects are possible when coupled normal modes of the nanoshell and core regions exhibit resonances close to each other in the energy spectrum. Thus the refractive index along with the dimensions of nanoshells that allow such behavior becomes crucial. In other spectral regions, the optical properties are not remarkably different from those of dielectric homogeneous spheres [20, 27]. Note that such particles can also exhibit directional scattering typically in the forward or backward directions in these significant spectral regions, which is a useful property for optical antennas [28]. This classical behavior has interesting quantum-mechanical interpretations that are potentially useful in single-photon communication applications. In the appendix, we also present a simple yet fundamental phase–magnitude relationship of the spherical scattering coefficients of homogeneous or layered dielectric spheres in generality.

We have decomposed the extinction spectra of nanoshell particles using the coefficients of the spherical modes in the well-known Lorenz–Mie theory [29]; the magnitude and phase of mode coefficients a_n, b_n for the external scattered field; c_n, d_n for the normal modes of the core region; and f_n, g_n, v_n, w_n for the normal modes of the shell region. The properties of the scattered field and resulting absorption/scattering are typically studied using mode coefficients of the external field a_n, b_n. The origin of such effects can also be elucidated using interference of normal modes of the core and shell regions that are coupled by boundary conditions. We highlight this effect with realistic nanospheres in water such as a dielectric core of silica which is very stable in nature [30, 31], and a shell of titania which is an unremarkable non-absorbing material in the visual spectrum, though strongly absorbing in the UV [32, 33]. It is observed that hollow titania nanoshells also exhibit similar but weaker behavior in the absence of the silica core. Equally, homogeneous spheres of titania or silica, or an imaginary effective material representing titania and silica, do not exhibit similar effects (see figures S1 and S2, available online at stacks.iop.org/JOPT/19/075603/mmedia). Numerical results also suggest that these interference effects can survive size-dispersion in actual realization of materials while allowing spectral tunability based on the nominal geometrical parameters.

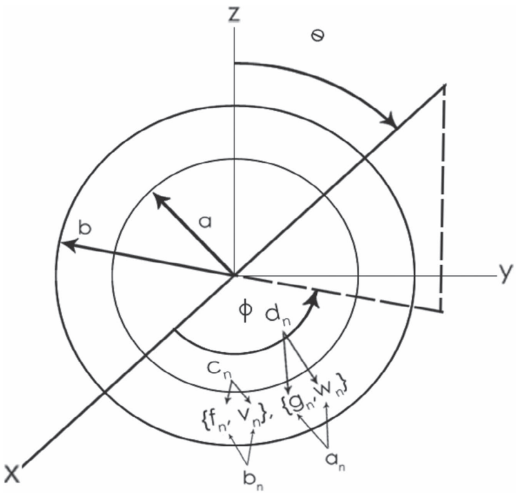

Figure 1. Schematic of the coordinate system used.

2. Methods

2.1. Analytical model

Consider a linearly polarized electromagnetic wave incident on a core–shell nanosphere with inner radius a and outer radius b (figure 1). The incident electric vector is polarized in the direction of the x axis and the direction of propagation of the incident wave is along the positive z axis. In spherical coordinates, if the amplitude of the incident wave at the origin is E_0, then the incident field E_i, H_i, the electromagnetic field in the core region E_1, H_1, the scattered field E_3, H_3 and the electromagnetic field in the shell region E_2, H_2 can be expressed in spherical harmonics using the normal modes of a sphere [21, 29] (see appendix). Here a_n and b_n denote the coefficients of scattered field, f_n, g_n, v_n, w_n represent the coefficients of normal modes in shell region and c_n, d_n the coefficients of normal modes of the core region respectively (see equations (5)–(12) in the appendix).

The extinction and scattering cross-sections are given by

$$C_{\text{ext}} = \frac{2\pi}{k^2}\sum_{n=1}^{\infty}(2n+1)\mathbb{R}(a_n + b_n) \tag{1}$$

$$C_{\text{sca}} = \frac{2\pi}{k^2}\sum_{n=1}^{\infty}(2n+1)(|a_n|^2 + |b_n|^2) \tag{2}$$

$$C_{\text{abs}} = C_{\text{ext}} - C_{\text{scat}}. \tag{3}$$

Efficiency $Q = \frac{C}{\pi b^2}$ and specifically the efficiency of the backscattering Q_b is

$$Q_b = \frac{1}{4\pi}\left[\frac{1}{k^2 b^2}\left|\sum_n (2n+1)(-1)^n(a_n - b_n)\right|^2\right] \tag{4}$$

where b is the radius of the sphere; note the factor '4 π' included here, which means that the differential scattering

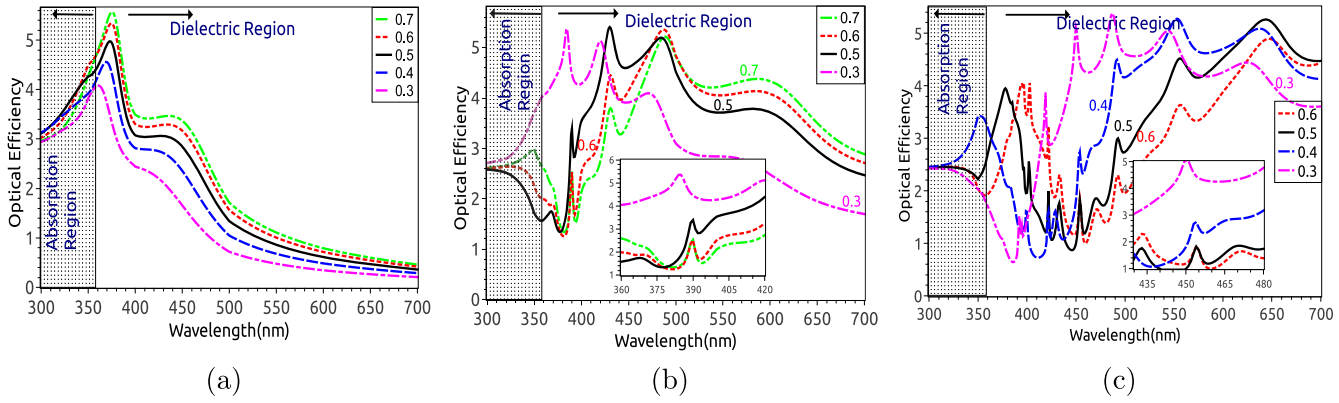

Figure 2. Extinction spectra as a function of free-space wavelength for silica–titania spheres in water at different shell ratios 0.3 to 0.7 (given by the ratio of the thickness of the shell and outer radius of the particle); (a) 180 nm diameter, (b) 360 nm diameter, (c) 600 nm diameter. The refractive index of the materials and extinction spectra for homogeneous spheres of silica, titania and their effective-media approximations are presented in supplementary material for reference.

cross-section at $\theta = 180^\circ$ is used to calculate Q_b. This additional factor is sometimes ignored to express the relative backscattering cross-section scaled to represent the total surface area of the particle [21]. Also, in the above equation, the removal of the antisymmetric operator $(-1)^n$, and a change to the sum of the scattering constants instead of their difference, will provide us with the forward scattering efficiency.

The final solutions for mode coefficients a_n, b_n are well known, and expressions to evaluate c_n, d_n, f_n, g_n, v_n, w_n can be easily derived as well (equations (23)–(28) in the appendix). The numerical evaluations of cross-sections using the above Lorenz–Mie formalism [21, 34, 35] were also verified and complemented by numerical volume integral methods such as discrete dipole approximation [36]. All the simulations were made with water, as an ambient medium of permittivity 1.77. These results of internal polarization are also used in elucidating the physics in the next section. As given by equations (5) and (6), we studied nanoshells illuminated by plane electromagnetic waves. We assume the titania is of anatase phase and the dispersive permittivity of anatase is different from its rutile phase [32, 33, 37, 38] (see supplementary material for the refractive indices of the materials used).

3. Results and discussion

Figure 2 shows the extinction spectra of silica–titania spheres of three increasing dimensions with varying ratios of thickness of shell and radius of particle. As mentioned before, the larger shells exhibit non-intuitive spectra which we show later to be due to interference effects better explained by the normal mode coefficients. The 180 nm diameter particles (represented in figure 2(a)) are unremarkable as they show a Rayleigh-scattering-type $\frac{1}{\lambda^4}$ behavior for $\lambda > 450$ nm as expected, followed by an indication of interference structure around the optical efficiency of 2 for 400 nm $< \lambda <$ 450 nm. Light of smaller wavelengths ($\lambda <$ 350 nm) is strongly absorbed by titania and the extinction spectra show a saturation behavior based on the thickness of the shells [39]. The 360 nm diameter particles (represented in figure 2(b)) exhibit a similar unremarkable Mie–Rayleigh behavior for wavelengths larger than 500 nm based on their larger size. On the other hand, an abrupt reduction in optical efficiency to ∼1.5 for the spectral range 350–430 nm range is observed. This efficiency is four times smaller than that of the smaller 180 nm sphere of similar constitution, and note that while both titania and silica are in fact mostly non-absorbing in this energy spectrum, the lack of stronger scattering for the larger particles seems anomalous. Weak absorption close to the absorption edge at 350 nm significantly enhances the typical interference structure in the extinction spectrum of a dielectric particle, resulting in this sharp asymmetric resonance around 370 nm. A similar more broadband effect for the larger sphere of 600 nm diameter (represented in figure 2(c)) is observed, which exhibits both a broader transparency (at $\lambda \sim 450$ nm) and another resonance (at $\lambda \sim 370$ nm). The tunability of this transparency using approximately the core–shell ratios of the particle are highlighted in these results. Other results showing that this effect is only weakly sensitive to the outer diameter of the particle are shown in the supplementary information (figure S1c). For a more qualitative investigation, we present further numerical results of the nanoshells where the thickness of the shell is half of the radius of the particle. In fact, the phase of oscillations of internal polarizations in the core–shell structure (with respect to incident field) shown in figure 3 indicates a non-trivial effect. At higher ($\lambda = 320$ nm) and lower ($\lambda = 425$ nm) energies the wave nature of the internal polarization is apparent (figures 3 and 3(b)); but at the critical wavelength of ∼370 nm the oscillations of the polarizations are neither like a passing nor a whispering gallery wave (figure 3(c)).

The magnitude of the spherical mode coefficients a_n, b_n plotted in figure 4 emphasizes the significance of the higher-order non-dipolar modes, especially for larger nanoshells of 600 nm diameter. This is evident from the magnitude of the normal mode coefficients numbered 2–12; the dipolar modes are represented by coefficients numbered 1. An analysis of mode constants a_n and b_n shows that large changes in magnitude occur in many modes in the same regions of the

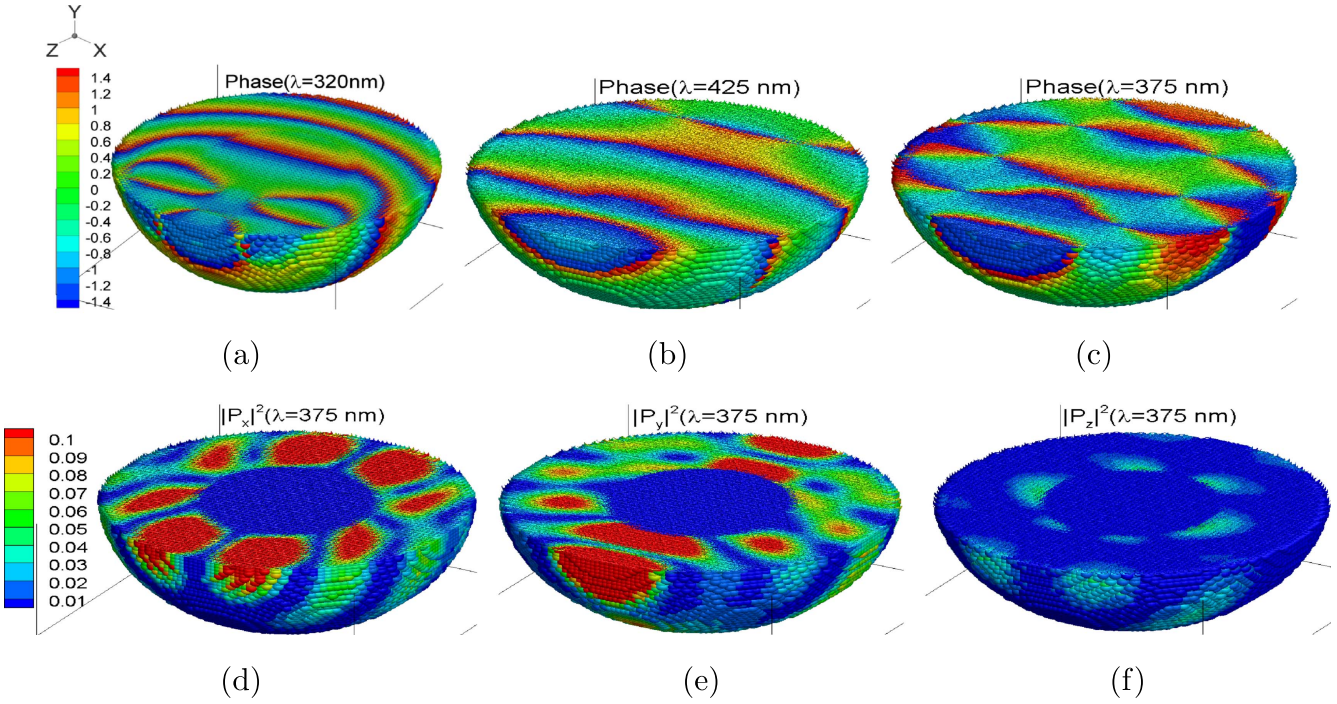

Figure 3. The top row shows the phase of polarization oscillations (in radians) with respect to the incident field (Y-polarized plane wave propagating in Z). The second row is the relative internal energy distribution. The 360 nm silica–titania core–shell particle of 0.5 shell ratio is sectioned at the $Y = 0$ plane to display a hemisphere and its internal distributions of polarizations. (a) Phase distribution of $\hat{P}_y$ at $\lambda = 320$ nm. (b) Phase distribution of $\hat{P}_y$ at $\lambda = 425$ nm. (c) Phase distribution of $\hat{P}_y$ at critical $\lambda = 375$ nm. At $\lambda = 375$ nm: (d) $|P_x|^2$. (e) $|P_y|^2$. (f) $|P_z|^2$. Note that a similar plot of phase (in radians) and relative energy distribution for 600 nm nanospheres is presented in the supplementary material.

spectrum. A cumulative effect of these large changes in magnitude of scattering constants is reflected in the extinction/scattering spectra in figure 2. This is due to the fact that the extinction cross-section is also given by the scattering cross-section of a dielectric particle (equation (2)), and the total scattering cross-section is just a sum over cross-sections of all modes. This results in a fundamental relationship between the phase and magnitude of the scattering coefficients (see appendix). The origin of this interference structure in spectra of a_n and b_n of a nanoshell particle requires further analysis of the internal TE and TM modes of the shell and core region.

In the case of spherical particles, large variations in spectra can be broadly due to two types of interference effects. The first is a ripple structure that is attributed to the maxima and minima in the forward scattering of a dielectric particle with a change in wavelength of incident light. This manifests for dielectric particles of size on the order of wavelength with a relative refractive index <2 and these are typically elucidated by the behavior of the Ricatti–Bessel functions and their ratios embedded in the boundary conditions (equations (15)–(22)). The other, sharper, effect manifests when there is a spectral overlap of resonance of two underlying modes that interact, a sharp resonance and a constant background. Let the amplitudes of oscillation of two such modes be represented by two phasors; the amplitude of a sharp Lorentzian resonance with a negligible damping reduces to $1/(\omega - \omega_o)$ while the broad background is $1/(i\Gamma)$. Note that their phases are zero and $\pi/2$ radians respectively. Thus when the phases are offset by $\pi/2$ radians away from the resonance, they add as two non-interacting modes do. But around resonance, the phases do align in a small region of the spectrum during the cross-over of the resonating phasor from zero to π, and this constructive addition of amplitudes results in an asymmetric resonance of magnitude $(\omega - \omega_o + \Gamma)^2/(\omega - \omega_o)^2 + \Gamma^2)$. This effect can also manifest when two coupled modes, like those of the core and shell modes, exhibit a spectral overlap of resonance. Here, their typical forced-driven relationship implies a phase offset of $\pi/2$ between modes of the core and shell in most regions of the spectrum. But any overlap of resonances aligns the phases in a small region of spectrum and interference effects appear (see figure S7 in the supplementary material for overlaps in phase of constants c, f and v).

When magnetic and electric modes overlap in magnetic spheres and oligomers of coupled dielectric spheres, magnetic-electric interference can result in Fano-type spectra. Recently, this effect was also shown to be possible in a single high-index homogeneous sphere due to spectral overlaps between the internal electric and magnetic resonances (represented by spectra of constants c_n, d_n) [40]. Also, one or more modes of a conducting particle can exhibit addition and cancellation with other mode phasors $(a_n + b_n)$, indicating interacting currents. Resulting sharp spectral features of metal particles have been referred to as plasmonic Fano resonances. For example, the overlapping electric resonances of the first two modes of a small plasmonic particle represented by scattering constants a_1, a_2 results in Fano profiles in spectra of the forward and backward scattering cross-sections [25]. As

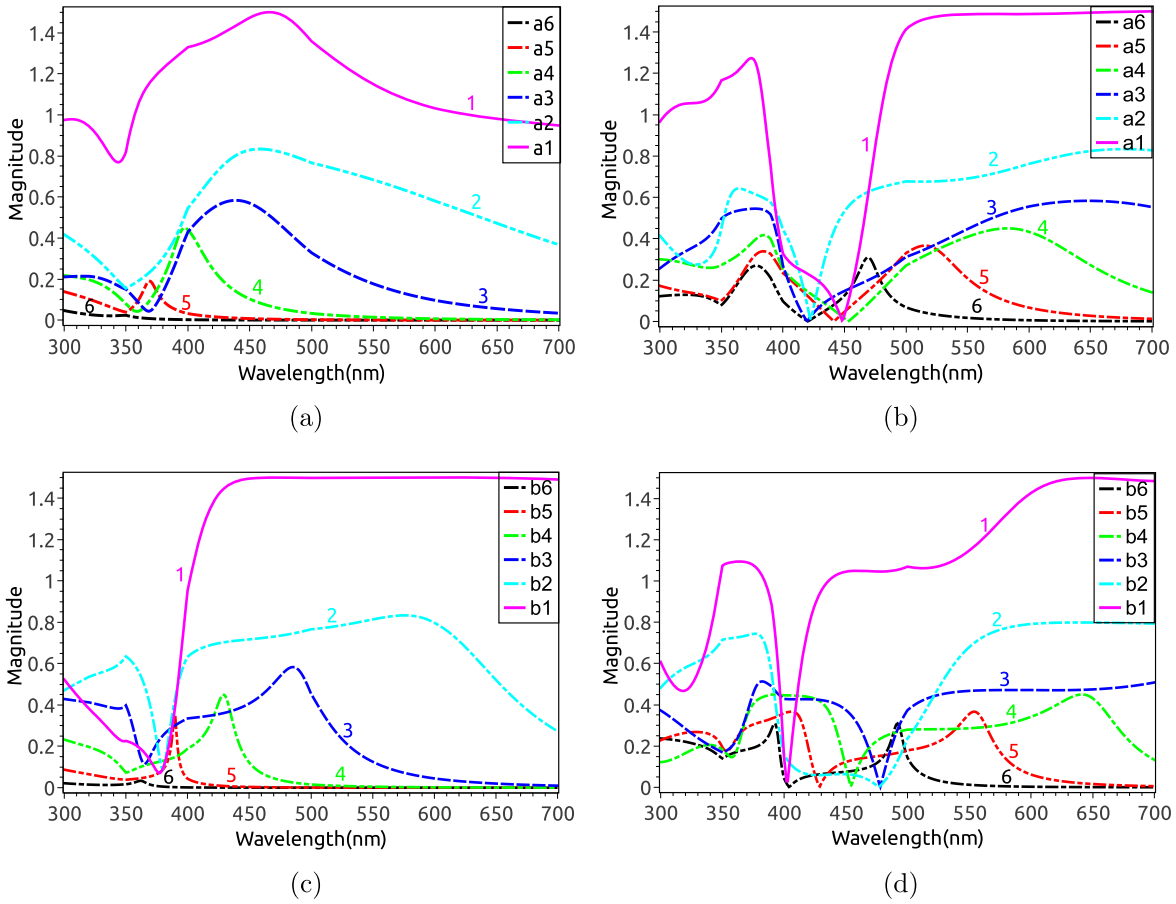

Figure 4. (a–d) Normalized distribution of magnitude of spherical mode coefficients ($E_n * a_n$, $E_n * b_n$) for 360 nm (on the left side) and 600 nm (on the right side) diameter particles of 0.5 shell ratio, as a function of free-space wavelength, where $E_n = \frac{2n+1}{n(n+1)}$. The magnitude of other mode coefficients b_n, d_n, g_n, w_n and higher modes of a_n and f_n (for $n = 7$ to 12) are plotted separately in the supplementary material for clarity.

mentioned before, even a homogeneous dielectric particle of index <2 exhibits an interference/ripple structure in its extinction spectra. But the typically shallow ripples in spectra of magnitudes of a_n, b_n of the relatively low-index dielectric particles on the order of wavelength in size have been uninteresting for applications. We show that when the ripple resonances of core and shell overlap, larger spectral structures in the magnitudes of scattering coefficients a_n and b_n are indeed possible. A core–shell particle allows such an overlap of resonances even when the modes of the core or shell alone do not overlap with each other for a particle with relatively low refractive index. This spectral signature is evident in the magnitudes of the scattering constants a_n and b_n as an enhanced ripple structure. This can be explained by the interference of the core and shell modes, which is similar to the cases of the Fano effects in high-index and metallic homogeneous spheres, as we discuss below.

While a_n and b_n denote the normal modes for the scattered field, f_n, g_n, v_n, w_n represent the transverse electric (TE) and magnetic (TM) modes of the shell region and c_n, d_n the core region respectively (refer to equations (5)–(12)). The distribution of all the mode coefficients in terms of their magnitude and phase are provided in the supplementary information. The overlaps of the TE and TM mode number 1 of the core–shell are plotted in figures 5(a) and (b) respectively. Note that c_n, f_n and v_n are the complementary mode coefficients that are coupled to the spectra of b_n by the boundary conditions (see appendix). Specifically, c_n represents both the incoming and outgoing TM waves in the core, f_n represents the incoming waves while v_n represents the outgoing TM waves of the shell. The other set d_n, g_n and w_n are similarly related to the spectra of a_n and TE modes. These four constants along with the driving incident field can be represented by five phasors of the electric modes (or magnetic modes in the case of c_n, f_n, v_n and b_n) of the three regions, for any mode number n. This contrasts with only a total of three phasors for each mode number of a homogeneous particle. When a TE resonance of the core (d_n) overlaps with the resonance of a TE mode of the shell (either outgoing or incoming waves represented by w_n or g_n), a sharp change in response of the other mode of the shell occurs. This is accompanied by a large spectral change in response of the scattering from the particle in terms of TE scattering constant a_n. This behavior adds to what would otherwise be typical ripple spectra of a homogeneous sphere.

To illustrate this effect, figures 5(a) and (b) plot the spectra of the modes of core and shell, followed by figure 5(c). Figure 5(c) provides scattering constant $a1$ that would be expected for a homogeneous sphere of an effective refractive

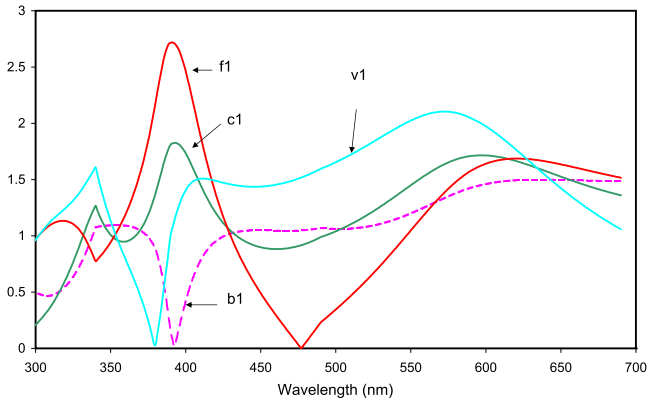

(a)

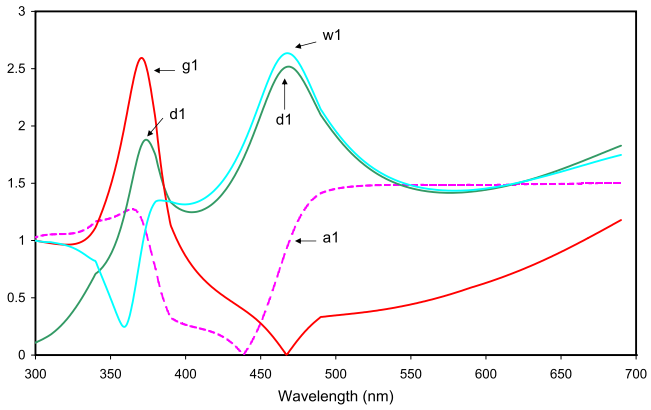

(b)

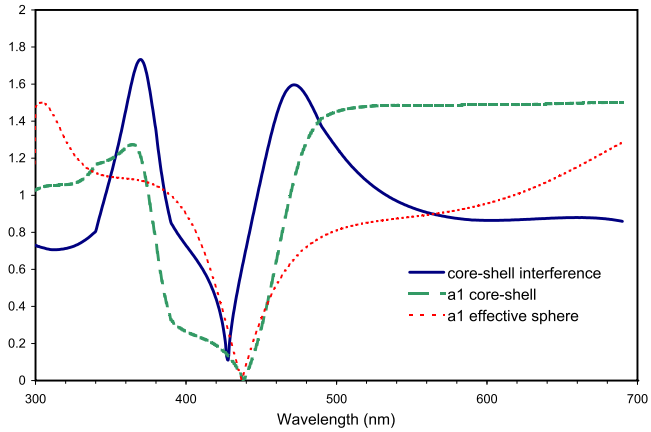

(c)

Figure 5. (a) Spectra of TM1 modes of the core and shell for the 600 nm diameter particle of 0.5 shell ratio, as a function of free-space wavelength. Note that these coefficients were scaled by $E_n = \frac{2n+1}{n(n+1)}$ which is $3/2$ for $n = 1$. (b) Spectra of TE1 modes of core and shell for the 600 nm diameter particle of 0.5 shell ratio. Note that these coefficients were scaled by $E_n = \frac{2n+1}{n(n+1)}$ which is $3/2$ for $n = 1$. (c) Interference of core–shell modes and effect on TE1 scattering coefficient a_1: comparison with a homogeneous sphere of the same effective refractive index. Amplitude of the core–shell interference is calculated using the energy imbalance across the shell boundaries by the incoherent sum $|(1 + |g_1|^2 - |w_1|^2 - |a_1|^2)|^{1/2}$.

index by volume for the given core–shell sphere. The scattering constant $a1$ is also plotted with an overlay of the spectral strength of interference among TE modes of the core and shell. It is apparent that the spectra of the TE mode number 1 are significantly enriched by the interference of the core and shell modes. Note that the peak interference occurs in a spectral region around the overlapping resonance peaks of the core and shell. The full extinction spectra of the effective index homogeneous spheres are provided in the supplementary information (figure S2 a–c), and the peak–valley ratio in the spectra of this homogeneous sphere is enhanced by a factor of more than 2 in the core–shell sphere. A similar effect and a marginally smaller factor of enhancement is exhibited by a hollow titania shell of the same dimensions (figure S2 (d–f) in the supplementary material). In lossy conducting particles the resonances in modes of different numbers n are indeed coupled by currents, which makes other interference effects between different mode numbers possible, and is not discussed further here.

A significant point is that in the typical Fano interaction between electric and/or magnetic modes of a homogeneous high-index and metallic sphere, a constant background (incident wave) appears either as a complete forward or a complete backward scattering, between resonances in the spectrum. A similar maximization of the backscattering component in the extinction at $\lambda \sim 460$ nm is noteworthy for the 600 nm particle (refer to equation (4) in the analytical model for an explanation of backscattering efficiency). Backscattering efficiency are plotted in figures 6(a) and (b) for two different particles discussed in detail. Backscattering can be complete for point-like dipoles and thus equal the total scattering cross-section [25]; here even a large core–shell structure would exhibit this limiting behavior for incident photons of particular energy.

To summarize, the interference resonances of homogeneous dielectric spheres simply understood as the interference of forward-scattered and incident light becomes a richer phenomenon in nanoshells. The large overlap between the complementary TE and TM modes of shell and core regions, possible in all-dielectric particles, provides an alternate avenue for achieving useful optical properties in nanoscale materials without the absorption accompanying plasmonic nanostructures or high-index materials.

Appendix A. Coefficients of spherical mode expansions

Continuing from section 2, the vector spherical harmonics using various normal modes M, N are given by [21]

$$E_{\mathrm{i}} = E_0 \sum_{n=1}^{\infty} \mathrm{i}^n \frac{2n+1}{n(n+1)} (M_{o1n}^{(1)} - \mathrm{i} N_{\mathrm{e}1n}^{(1)}) \tag{5}$$

$$H_{\mathrm{i}} = \frac{-k}{w\mu} E_0 \sum_{n=1}^{\infty} \mathrm{i}^n \frac{2n+1}{n(n+1)} (M_{\mathrm{e}1n}^{(1)} + \mathrm{i} N_{o1n}^{(1)}) \tag{6}$$

$$E_1 = \sum_{n=1}^{\infty} E_n (c_n M_{o1n}^{(1)} - \mathrm{i} d_n N_{\mathrm{e}1n}^{(1)}) \tag{7}$$

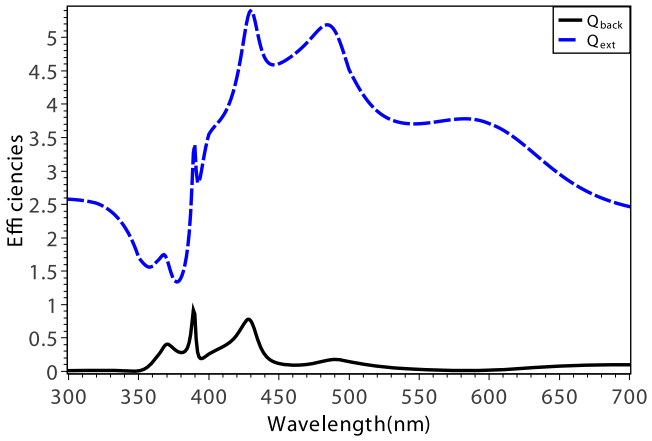

(a)

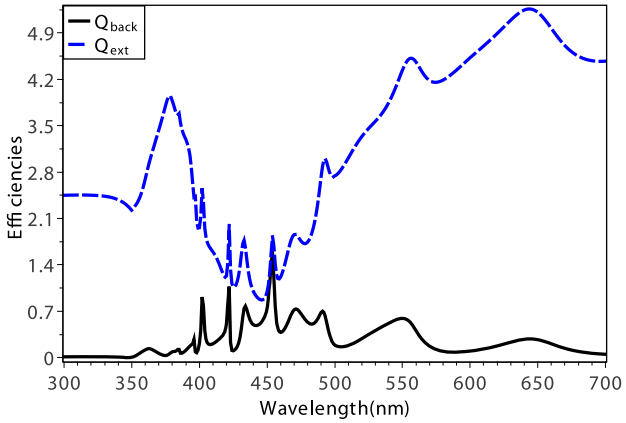

(b)

Figure 6. (a) Extinction and backscattering efficiency spectra of the 360 nm diameter particle of 0.5 shell ratio. (b) Extinction and backscattering efficiency spectra of the 600 nm diameter particle of 0.5 shell ratio.

$$H_1 = \frac{-k_1}{\omega\mu_1}\sum_{n=1}^{\infty} E_n(d_n M_{e1n}^{(1)} + \mathrm{i}c_n N_{o1n}^{(1)}) \tag{8}$$

$$E_2 = \sum_{n=1}^{\infty} E_n[f_n M_{o1n}^{(1)} - \mathrm{i}g_n N_{e1n}^{(1)} + v_n M_{o1n}^{(2)} - \mathrm{i}w_n N_{e1n}^{(2)}] \tag{9}$$

$$H_2 = \frac{-k}{w\mu_2}\sum_{n=1}^{\infty} E_n[g_n M_{e1n}^{(1)} + \mathrm{i}f_n N_{o1n}^{(1)} + w_n M_{e1n}^{(2)} + \mathrm{i}v_n N_{o1n}^{(2)}] \tag{10}$$

$$E_3 = \sum_{n=1}^{\infty} E_n(\mathrm{i}a_n N_{e1n}^{(3)} - b_n M_{o1n}^{(3)}) \tag{11}$$

$$H_3 = \frac{k}{\omega\mu}\sum_{n=1}^{\infty} E_n(\mathrm{i}b_n N_{o1n}^{(3)} + a_n M_{e1n}^{(3)}) \tag{12}$$

where $\mathrm{i} = \sqrt{-1}$; $E_n = \mathrm{i}^n E_0 \frac{2n+1}{n(n+1)}$; ω is the angular frequency; k and k_1 are the wave number in the sphere given by $\frac{2\pi m}{\lambda_0}$ $\frac{2\pi m_1}{\lambda_0}$ respectively; λ_0 is the wavelength in vacuum, m_1 and m_2 are the refractive indices of the core and shell relative to the surrounding medium; μ, μ_1 and μ_2 are the permeabilities of surrounding medium, core, shell respectively; and a_n, b_n, c_n, d_n, f_n, g_n, v_n, w_n are the spherical mode coefficients. After applying the boundary conditions for a sphere with inner radius a and outer radius b,

$$(E_2 - E_1) \times \hat{\epsilon_r} = 0\,(H_2 - H_1) \times \hat{\epsilon_r} = 0 \;\text{ where, } r = a \tag{13}$$

$$(E_3 + E_\mathrm{i} - E_2) \times \hat{\epsilon_r} = 0\,(H_3 + H_\mathrm{i} - H_2) \times \hat{\epsilon_r} = 0 \;\text{ where, } r = b \tag{14}$$

we get the following equations in coefficients a_n, b_n, c_n, d_n, f_n, g_n, v_n, w_n [22].

$$f_n m_1 \psi_n(m_2 x) - v_n m_1 \chi_n(m_2 x) - c_n m_2 \psi_n(m_1 x) = 0 \tag{15}$$

$$w_n m_1 \chi_n'(m_2 x) - g_n m_1 \psi_n'(m_2 x) + d_n m_2 \psi_n(m_1 x) = 0 \tag{16}$$

$$v_n \mu_1 \chi_n'(m_2 x) - f_n \mu_1 \psi_n'(m_2 x) + c_n \mu_2 \psi_n'(m_1 x) = 0 \tag{17}$$

$$g_n \mu_1 \psi_n(m_2 x) - w_n \mu_1 \chi_n(m_2 x) - d_n \mu_2 \psi_n(m_1 x) = 0 \tag{18}$$

$$m_2 \psi_n'(y) - a_n m_2 \xi_n'(y) - g_n \psi_n'(m_2 y) + w_n \chi_n'(m_2 y) = 0 \tag{19}$$

$$m_2 b_n \xi_n(y) - m_2 \psi_n(y) + f_n \psi_n(m_2 y) - v_n \chi_n(m_2 y) = 0 \tag{20}$$

$$\mu_2 \psi_n(y) - a_n \mu_2 \xi_n(y) - g_n \mu \psi_n(m_2 y) + w_n \mu \chi_n(m_2 y) = 0 \tag{21}$$

$$b_n \mu_2 \xi_n'(y) - \mu_2 \psi_n'(y) + f_n \mu \psi_n'(m_2 y) - v_n \mu \chi_n'(m_2 y) = 0. \tag{22}$$

These boundary conditions and final solutions for mode coefficients a_n, b_n are well known [21] and coefficients c_n, d_n, f_n, g_n, v_n, w_n can be similarly derived using the above boundary conditions.

Let $D_x = \frac{\psi_n'(m_2 x)}{\psi_n(m_2 x)}$ $D_y = \frac{\psi_n'(m_2 y)}{\psi_n(m_2 y)}$

$$c_n = \frac{m_1 D_x v_n \chi_n(m_2 x) - m_1 v_n \chi_n'(m_2 x)}{m_1 \psi_n'(m_1 x) - m_2 D_x \psi_n(m_1 x)} \tag{23}$$

$$d_n = \frac{w_n m_1 \chi_n'(m_2 x) - m_1 D_x w_n \chi_n(m_2 x)}{m_1 D_x \psi_n(m_1 x) - m_2 \psi_n'(m_1 x)} \tag{24}$$

$$f_n = \frac{v_n \chi_n(m_2 y) + m_2 \psi_n(y) - m_2 b_n \xi_n(y)}{\psi_n(m_2 y)} \tag{25}$$

$$g_n = \frac{w_n \chi_n(m_2 x) + d_n \psi_n(m_1 x)}{\psi_n(m_2 x)} \tag{26}$$

$$v_n = \frac{b_n \xi_n'(y) - \psi_n'(y) - D_y m_2 b_n \xi_n(y) + D_y m_2 \psi_n(y)}{\chi_n'(m_2 y) - D_y \chi_n(m_2 y)} \tag{27}$$

$$w_n = \frac{a_n m_2 \xi_n'(y) + D_y \psi_n(y) - D_y a_n \xi_n(y) - m_2 \psi_n'(y)}{\chi_n'(m_2 y) - D_y \chi_n(m_2 y)} \tag{28}$$

where μ is assumed to be constant for the materials and $x = ka$, $y = kb$. Riccati–Bessel functions are given as $\chi_n(\rho) = -\rho y_n(\rho)$, $\psi_n(\rho) = \rho j_n(\rho)$ and $\xi_n(\rho) = \rho h_n^{(1)}(\rho)$. $\chi_n'(\rho)$, $\psi_n'(\rho)$, $\xi_n'(\rho)$ represent the differentials of the same with respect to the argument in the parenthesis. Here, $j_n(\rho)$ is defined as $\sqrt{\frac{\pi}{2\rho}} j_{n+\frac{1}{2}}$, where $j_{n+\frac{1}{2}}$ is the Bessel function of the first kind. $y_n(\rho)$ is defined as $\sqrt{\frac{\pi}{2\rho}} y_{n+\frac{1}{2}}$, where $y_{n+\frac{1}{2}}$ is the Bessel function of the second kind and $h_n^{(1)}(\rho)$ is known

as the spherical Hankel function, which is defined as $j_n(\rho) + iy_n(\rho)$. The numerical evaluations of cross-sections using the above Lorenz–Mie formalism [21, 35, 36] were also verified and complemented by numerical volume integral methods such as discrete dipole approximation [37]. All the simulations were performed with water, as an ambient medium of permittivity 1.77. These results of internal polarization are also used in elucidating the physics in the previous section.

Appendix B. Phase–magnitude relationship of scattering coefficients for dielectric particles

From equations (1) and (2), equality of the following series in the scattering coefficients results for any dielectric sphere with an arbitrary number of layers

$$\sum_{n=1}^{\infty}(2n+1)\mathbb{R}(a_n+b_n)=\sum_{n=1}^{\infty}(2n+1)(|a_n|^2+|b_n|^2). \tag{29}$$

For the above to hold true in generality for all dielectric properties and dimensions of particles, each coefficient should independently satisfy the above relation, resulting in

$$\mathbb{R}(a_n)=|a_n|^2 \tag{30}$$

showing that

$$|a_n|=\cos\theta_n \tag{31}$$

and

$$a_n=\cos^2\theta_n+\frac{\mathrm{i}}{2}\sin 2\theta_n \tag{32}$$

where θ_n is the phase of a_n (and the above relations are equally applicable to b_n as well). This reemphasizes the known physical conclusions that $|a_n| \leqslant 1$. Secondly, the phase of oscillation of the polarized particle relative to an incident plane wave is $0 \geqslant \theta \leqslant \pi$, as the period of the above circular trace is only π. Note that the trace of scattering coefficients a_n and b_n in the complex plane is given by a circle with a center at (0.5, 0i) and a radius 0.5, for any mode n of any dielectric particle (given by equation (32)). This relation can be exploited for fast evaluation of scattering from dielectric particles with a distribution in the refractive index or the dimensions, an exercise that may be shown elsewhere.

References

[1] Jain P K and El-Sayed M A 2007 Surface plasmon resonance sensitivity of metal nanostructures: physical basis and universal scaling in metal nanoshells *J. Phys. Chem.* C **111** 17451–4

[2] Xu Q, Liu F, Meng W and Huang Y 2012 Plasmonic core–shell metal-organic nanoparticles enhanced dye-sensitized solar cells *Opt. Express* **20** 898–907

[3] Sikdar D, Rukhlenko I D, Cheng W and Premaratne M 2013 Optimized gold nanoshell ensembles for biomedical applications *Nano. Res. Lett.* **8** 142

[4] Hao F and Nordlander P 2007 Enhanced tunability and linewidth sharpening of plasmon resonances in hybridized metallic ring/disk nanocavities *Phys. Rev.* B **76** 245417

[5] Yong K, Sahoo Y, Swihart M T and Prasad P N 2006 Synthesis and plasmonic properties of silver and gold nanoshells on polystyrene cores of different size and of gold-silver core–shell nanostructures *Colloids Surf.* A **290** 89–105

[6] Miroshnichenko A E and Kivshar Y S 2012 Fanoresonances in all-dielectric oligomers *Nano. Lett.* **12** 6459–63

[7] Fedotov V A, Rose M M, Prosvirnin S L, Papasimakis N and Zheludev N I 2007 Trapped-mode resonances in planar metamaterials with a broken structural symmetry *Phys. Rev. Lett.* **99** 147401

[8] Yang J, Rahmani M, Teng J H and Hong M H 2012 Magnetic-electric interference in metal-dielectric-metal oligomers: generation of magneto-electric Fano resonance *Opt. Mater. Express* **2** 1408–14

[9] Staude I *et al* 2013 Tailoring directional scattering through magnetic and electric resonances in subwavelength silicon nanodisks *ACS Nano* **7** 7824–32

[10] Staude I, Khardikov V V, Fofang N T, Liu S, Decker M, Neshev D N, Luk T, Brener I and Kivshar Y S 2015 Shaping photoluminescence spectra with magneto-electric resonances in all-dielectric nanoparticles *ACS Photonics* **2** 172–7

[11] Pilat M J 1967 Optical efficiency factors for concentric spheres *Appl. Opt.* **6** 1555–8

[12] Kerker M, Wang D S and Giles C L 1983 Electromagnetic scattering by magnetic spheres *J. Opt. Soc. Am.* **73** 765–7

[13] Person S, Jain M, Lapin Z, Saenz J J, Wicks G and Novotny L 2013 Demonstration of zero optical backscattering from single nanoparticles *Nano. Lett.* **13** 1806–9

[14] Verre R, Yang Z J, Shegai T and Kal M 2015 Optical magnetism and plasmonic Fano resonances in metal-insulator-metal oligomers *Nano. Lett.* **15** 1952–8

[15] Laskar J M, Raj B and Philip J 2011 Enhanced transmission with tunable Fano-like profile in magnetic nanofluids *Phys. Rev.* E **84** 051403

[16] Owen J F, Chang R K and Barber P W 1981 Internal electric field distributions of a dielectric cylinder at resonance wavelengths *Opt. Lett.* **6** 540–2

[17] Owen J F, Barber P W, Dorain P B and Chang R K 1981 Enhancement of fluorescence induced by microstructure resonances of a dielectric fiber *Phys. Rev. Lett.* **47** 1075–8

[18] Hill S C and Benner R E 1986 Morphology-dependent resonances associated with stimulated processes in microspheres *J. Opt. Soc. Am.* B **3** 1509–14

[19] Balistreri M L M, Klunder J W, Blom F C, Driessen A, Hoekstra H W J M, Korterik J P, Kuipers L and Van Hulst N F 1999 Visualizing the whispering gallery modes in a cylindrical optical microcavity *Opt. Lett.* **24** 1829–31

[20] Thurn R and Kiefer W 1985 Structural resonances observed in the Raman spectra of optically levitated liquid droplets *Appl. Opt.* **24** 1515–9

[21] Bohren C F and Huffman D R 1983 *Absorption and Scattering of Light by Small Particles* (New York: Wiley)

[22] Affolter P and Eliasson B 1973 Electromagnetic resonances and Q-factors of lossy dielectric spheres *IEEE Trans. Microw. Theory Tech.* **MTT-21** 573–8

[23] Fano U 1961 Effects of configuration interaction on intensities and phase shifts *Phys. Rev.* **124** 1866

[24] Huffman D R 1977 Interstellar grains: the interaction of light with a small-particle system *Adv. Phys.* **26** 129–230

[25] Lukyanchuk B, Zheludev N I, Maier S A, Halas N J, Nordlander P, Giessen H and Chong C T 2010 The Fano resonance in plasmonic nanostructures and metamaterials *Nat. Mater.* **9** 707–15

[26] Chew H and Kerker M 1976 Abnormally low electromagnetic scattering cross sections *J. Opt. Soc. Am.* **66** 445–8
[27] Conwell P R, Barber P W and Rushforth C K 1984 Resonant spectra of dielectric spheres *J. Opt. Soc. Am.* **1** 62–7
[28] Novotny L 2007 Effective wavelength scaling for optical antennas *Phys. Rev. Lett.* **98** 266802
[29] Aden A L and Kerker M 1951 Scattering of electromagnetic waves from two concentric spheres *J. Appl. Phys.* **22** 1242
[30] Palik E D 1985 *Handbook of Optical Constants of Solids* (Cambridge, MA: Academic)
[31] Kitamura R, Pilon L and Jonasz M 2007 Optical constants of silica glass from extreme ultraviolet to far infrared at near room temperature *Appl. Opt.* **46** 8118–33
[32] Mergel D, Buschendorf D, Eggert S, Grammes R and Samset B 2000 Density and refractive index of TiO2 films prepared by reactive evaporation *Thin Solid Films* **371** 218
[33] Kim S Y 1996 Simultaneous determination of refractive index, extinction coefficient, and void distribution of titanium dioxide thin film by optical methods *Appl. Opt.* **35** 6703
[34] Mie G 1908 Contributions to the optics of diffuse media, especially colloid metal solutions *Ann. Phys., Lpz.* **25** 377–445
[35] Stratton J A 1941 *Electromagnetic Theory* (New York: McGraw-Hill)
[36] Draine B T and Flatau P J 1994 Discrete dipole approximation for scattering calculations *J. Opt. Soc. Am.* **11** 1491–9
[37] Mo S-D and Ching W Y 1995 Electronic and optical properties of three phases of titanium dioxide: rutile, anatase, and brookite *Phys. Rev.* B **51** 13023
[38] Prasai B, Cai B, Kyle U M, Lewis J P and Drabold D A 2012 Properties of amorphous and crystalline titanium dioxide from first principles *J. Mater. Sci.* **47** 7515–21
[39] Venkatapathi M, Dastidar S G, Bharath P, Roy A and Ghosh A 2013 Enhanced photo-absorption efficiency of incomplete nanoshells *Opt. Lett.* **38** 3275–8
[40] Tribelsky M I and Miroshnichenko A E 2016 Giant in-particle field concentration and Fano resonances at light scattering by high-refractive-index particles *Phys. Rev.* A **93** 053837